A Coherent Mixing Mechanism Explains the Photoinduced Nuclear Polarization in Photosynthetic Reaction Centers†

2 AUTHORS:

Tatyana Polenova
University of Delaware
88 PUBLICATIONS 1,759 CITATIONS

SEE PROFILE

Ann Mcdermott
Columbia University
100 PUBLICATIONS 4,019 CITATIONS

SEE PROFILE

A Coherent Mixing Mechanism Explains the Photoinduced Nuclear Polarization in Photosynthetic Reaction Centers[†]

Tatyana Polenova and Ann E. McDermott*

Columbia University, Department of Chemistry, New York, New York 10027

Received: May 18, 1998; In Final Form: September 15, 1998

Solid-state NMR spectra of Q-blocked photocycling photosynthetic reaction centers exhibit strongly enhanced lines. These peaks, for both carbon and nitrogen spectra, can be assigned to the primary donor bacteriochlorophyll special pair and the primary acceptor pheophytin. This paper concerns the mechanism by which the polarization develops. Previously reported simulations involving a radical pair mechanism (RPM) could achieve good agreement for the bacteriochlorophyll-containing electron donor, but not for the pheophytin acceptor. In this paper we focus on the N II and N IV nitrogens of the pheophytin acceptor, which we know are strongly directly polarized and for which we cannot explain the polarization by the RPM. To explain the strongly polarized acceptor signals, we propose a three-spin coherent mixing mechanism: nanosecond time scale coherent mixing of nuclear states and electron zero-quantum states are combined with chemical decay kinetics (back electron transfer) using the stochastic Liouville equation, to yield the density matrix for the radical pair states, $^1P^+\cdot H^-\cdot(t)$ and $^3P^+\cdot H^-\cdot(t)$. We solve the equation numerically for the yields of the ground state P (after back-electron transfer) and the molecular triplet ^3P, as well as the nuclear polarization associated with each of these yields. Nuclear polarization results from such a dynamical system only if the dipolar Hamiltonian is not fully truncated; terms involving nuclear raising and lowering operators must be retained. Nuclear polarization is computed for crystallites at a variety of (2500) randomly selected orientations with respect to the magnetic field, and polarized powder patterns and MAS spectra are simulated, showing good agreement with the experimental data. Several characteristics of this coherent mixing mechanism are described below that will help discern other experimental systems that are likely to develop large nuclear polarization. Unlike previous mechanisms, nuclear relaxation rates and electron−nuclear cross relaxation rates do not drive the development of polarization and therefore are not critical to the success of the scheme. The mechanism is driven by coherent evolution, and the critical kinetic parameters are the electron zero-quantum frequency, the hyperfine coupling, and the nuclear Zeeman terms which must be comparable (i.e., within 2 orders of magnitude) for optimal polarization to be observed. The chemical reaction constants are also critical to this scheme: the singlet decay constant must be slow enough to allow some evolution under the influence of the hyperfine interaction, and the triplet decay kinetics must be very different from the singlet decay constant to achieve net polarization. With the spectroscopic parameters reported for the photosynthetic reaction center, such an ideal matching of kinetic constants was not achieved except for specific orientations, and yet numerical simulations indicate that we can explain polarizations of up to $10^4 \times$ Boltzmann polarization (single turnover) and up to $10^5 \times$ Boltzmann polarization (steady-state case) with this mechanism. The anisotropy associated with the **g** and hyperfine tensors resulted in a highly anisotropic steady state polarization; the largest effect is expected for orientations for which anisotropic zero-quantum electron frequency (the difference of the **g** tensors of BChl and BPheo) is the smallest.

Introduction

NMR is a notoriously insensitive spectroscopic method, due to the poor Boltzmann polarization factors at thermal equilibrium. Micromoles or at least hundreds of nanomoles of material are required for most experiments, which makes NMR useless for many interesting problems. We have reported solid state NMR spectra that indicate strongly polarized nuclei can be made in photosynthetic reaction centers by simple CW illumination.[1−3] We would like to understand the mechanism by which this polarization is developed and predict whether such strongly enhanced signals might be possible in other systems. We also reported[4] that the well-known CIDNP or Radical Pair Mecha-

nism[5,6] may not be able to explain our data. Specifically, the strong polarization on the bacteriopheophytin electron acceptor species cannot be satisfactorily explained in the RPM mechanism. In the RPM, singlet and triplet species result from photochemistry with equal and opposite polarization. To achieve net polarization, relaxation of nuclei by a long lived paramagnetic intermediate is essential; coupled to the initial nuclear spin sorting, relaxation can produce net nuclear polarization. In the case of the photosynthetic reaction center it is difficult to explain the polarization we observed in such a scheme because the pheophytin species is 18 Å away from the only relevant relaxant, the long lived (100 μs) molecular triplet species.

Other mechanisms for producing polarization in radical or chromophore containing samples have been discussed in the

literature. DNP experiments[7] and its recent extensions[8−12] rely on "forbidden" nuclear−electron cross-relaxation processes. Optical pumping experiments involving circular polarization light sources can result in nuclear polarization for some gas phase species;[13] optical pumping also has exciting applications in the condensed phase,[14−16] reviewed in ref 17.

Recent EPR experiments indicate that coherent mixing of electrons and nuclei might give rise to peculiar nonthermal nuclear states and that such a mixing process could provide a fundamentally distinct way to produce large, nonthermal nuclear polarization.[18−21] In this paper we consider whether a coherent mixing mechanism involving two weakly coupled electrons and a strongly hyperfine coupled nucleus could provide an explanation for the polarized nuclei observed in the photosynthetic reaction center.

In the following we try to introduce what is new in the proposed mechanism is and why it is kinetically reasonable for the photosynthetic reaction center. The kinetic scheme of the reaction center is shown in Figure 1a and b. In Figure 1a, the electron spin states of the paramagnetic intermediates are indicated using the cone−vector pictures. The time evolutions of the nuclear spin states are shown in four stages in Figure 1b. Our simulations utilize the stochastic Liouville equation with an initial state consisting of an electronic singlet state (Figure 1a, state 1) and nonpolarized nuclei (stages 1 and 2 of Figure 1b). The inner two states for the electrons (singlet and zero sublevel of the triplet) are included, but the outer triplet states or double quantum states are omitted. This initial state is propagated with coherent mixing terms from the Zeeman interactions for both the electrons and the nucleus, weak dipolar, and *J*-couplings between the electrons, and a dipolar Hyperfine interaction between the nucleus and one of the electrons. The two nuclear states might be associated with different singlet−triplet mixing rates, due to contributions from the truncated hyperfine couplings. Thus the paramagnetic intermediates can exhibit substantial nuclear polarizations, but these species are not usually observable in an NMR experiment (stage 3, Figure 1b). These species return through chemical processes (e.g., back-electron transfer) to the diamagnetic ground electronic states, which are NMR observable (Figure 1b, stages 4 and 5). Nuclear polarization for the ground state species detected at long times (Figure 1b stage 5) is not expected if the back reactions for the singlet and the triplet form identical species: the net mixing process does not change the nuclear states but rather *temporarily* "sorts" nuclei and, after back electron transfer, produces molecular triplet and ground state with equal and opposite nuclear polarizations, as has been explained previously. The ground state species can exhibit nuclear polarization in this system under certain circumstances; however, if the photoproducts from the singlet and the triplet branch are distinct, or if the singlet and triplet species are subject to different relaxation mechanisms (relaxation during stage 4), as indicated in Figure 1. If the singlet and the triplet branches can be distinguished in these ways (or if time resolved experiments are performed to distinguish them), then net polarizations in the ground state can be observed, and often mechanistic information about the reaction can be attained.

The photosynthetic reaction center is a likely candidate for the spin sorting mechanism, but selective relaxation might not be relevant for the pheophytin species, due to the long distance between pheophytin and the molecular triplet ^{3}P. The proposed three spin mixing mechanism takes advantage of spin sorting in a very different way. For times after photon absorption long when compared with the triplet back electron reaction, but short

when compared with the singlet back reaction, the three spin system will temporarily exhibit a strong nuclear polarization (stage 3 of Figure 1). Species which have left the three spin system through back electron transfer to form the two products, the ground state and the molecular triplet, will be associated with an equal and opposite nuclear polarization. Thus, no net polarization develops. During this time interval the nuclei are sorted according to whether the species is biradical and is still in the three-spin system vs whether it is a molecular triplet or ground state (i.e., has left the three-spin system). The sorting viewed in this way, biradical vs recombined, provides a previously unrecognized window of opportunity: the dipolar hyperfine coupling can achieve *net action* on the spin system for this time interval via the *C* and *D* terms[7] which are associated with transverse (or raising and lowering) operators for the nuclei. The dipolar hyperfine coupling will act to recover balance (I_z) for the biradical states. Since the biradical states are selectively draining ^{3}P with nuclear state α, a net creation of α states will result. In this work we compute the trajectories of the biradical spin states, including one strongly coupled nucleus, and then calculate the nuclear polarization expected for the back electron transfer products: PN_z and ^3PN_z, assuming that the back electron transfers for both singlet and triplet states are first-order processes. The polarizations associated with the two long-lived species are not equal and opposite when the dipolar hyperfine interaction is substantial; thus the net polarization $N_z = PN_z + {}^3PN_z$ is nonzero, even without relaxation effects. We describe such a mechanism in a simplified case and then utilize this concept to simulate the spectra for the photosynthetic reaction center, wherein large effects are calculated.

Materials and Methods

All simulations were performed using Mathematica 3.0 (Wolfram, Inc.) for SGI and the corresponding notebooks and additional illustrations can be viewed at http://www.chem.columbia.edu/biophys/mcdhome.

Calculations of Time Trajectories of the Electron−Nuclear Spin Coherences. The time trajectories of the electron−nuclear spin coherences were calculated by solving the Stochastic Liouville equation (SLE)[22] for the density operator and computing the time dependencies of the observable operators, representing the electron−nuclear coherences responsible for generating the final nuclear polarization. For the radical pair, the triplet and the singlet decay processes can be introduced phenomenologically, and the resulting SLE takes the form[23−25]

$$\frac{d\hat{\rho}(t)}{dt} = -i/\hbar[[\mathbf{H}, \hat{\rho}(t)]_- - {}^1\!/_2 k_s[\hat{\mathbf{P}}^s, \hat{\rho}(t)]_+ - {}^1\!/_2 k_t[\hat{\mathbf{P}}^t, \hat{\rho}(t)]_+$$

(1)

where $\hat{\rho}(t)$ is the density operator, $\hat{\mathbf{H}}$ is the Hamiltonian, $\hat{\mathbf{P}}^s$ and $\hat{\mathbf{P}}^t$ are the singlet and the triplet projection operators, defined below, k_s and k_t are the singlet and the triplet decay rate constants, and $[\ ]_\mp$ are the commutator and anticommutator operators, respectively.

All the calculations were performed in a reduced high-field (product) basis set of the S−T$_0$ subsystem. In this basis set, the Hamiltonian, the density operator, and the electron and nuclear spin operators were written out as 4×4 matrixes consisting of two 2×2 blocks corresponding to the nuclear α and β states. Each of the 2×2 blocks contained the electron product basis functions αβ and βα. These basis functions
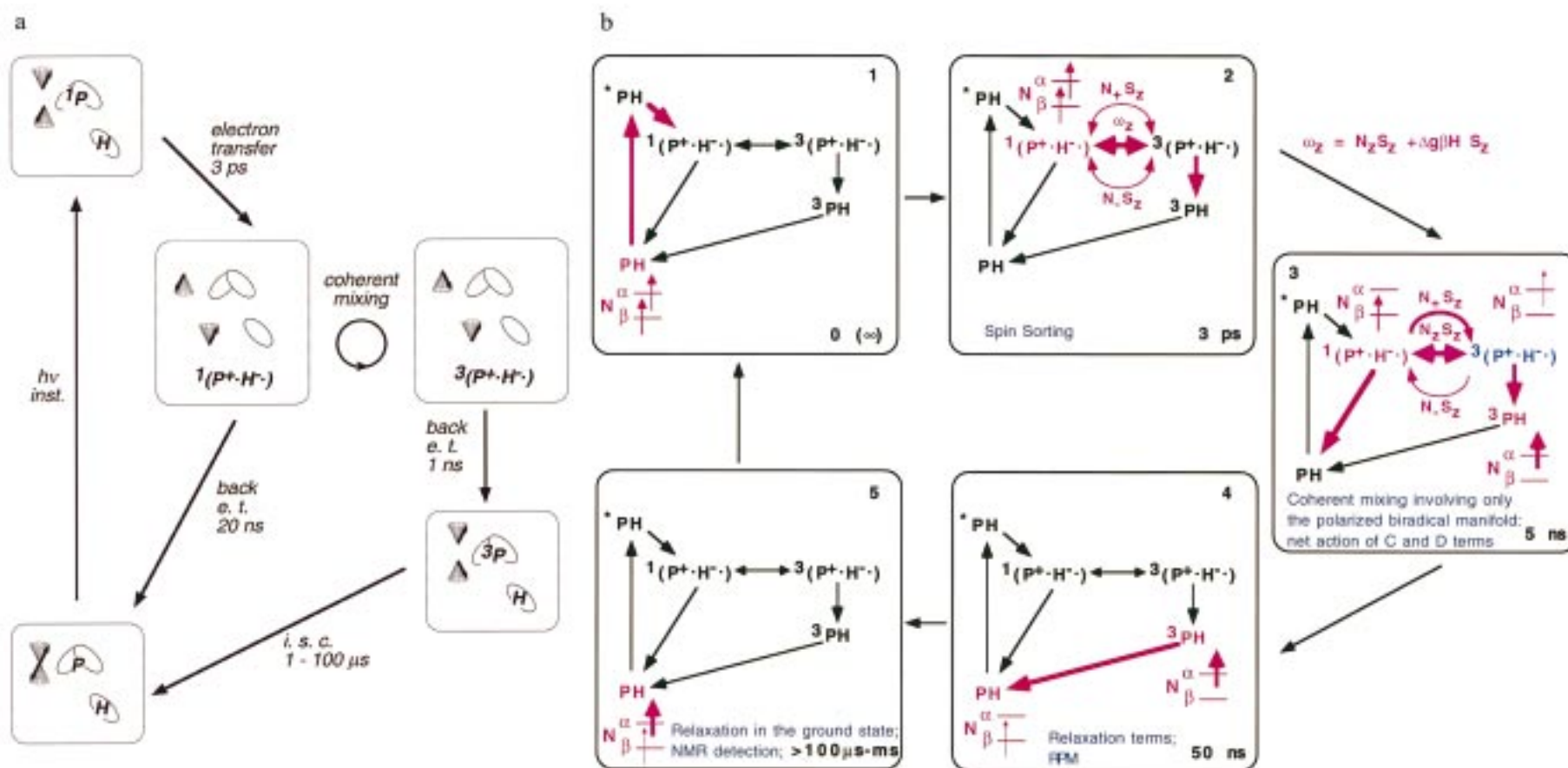
Figure 1. (a) Reaction scheme for Q-blocked photosynthetic reaction centers, with cones depicting the phase relationships between the two unpaired electrons in the radical pair. Figure (b) The sequence of diagrams illustrates the time evolutions of various nuclear spin states and nuclear polarizations associated with them in a RPM for a cyclic reaction, with reference to a single nitrogen nucleus on the pheophytin acceptor: (1) the ground state is populated and unpolarized at $t = 0$ and $t = \infty$; (2) the initial radical pair singlet is unpolarized and fully occupied at $t = 3$ ps; (3) the molecular triplet species and both radical pair states are populated and polarized at $t = 5$ ns; (4) at $t = 50$ ns the ground state is populated, with a preference for a nuclear beta state, and the molecular triplet is populated with a preference for nuclear alpha state but the sum of polarizations is nonzero; (5) from $t = 100$ μs onward all molecules are in the ground state and polarized; the decay of the polarization to its equilibrium value is determined by the nuclear T_1. For the case of the N-II and N-IV nitrogens of the pheophytin acceptor, in the orientations that give rise to the biggest polarization, there is a predilection for the radical pair triplet to be found with an ^{15}N alpha state since those orientations that have the smallest g value difference have a more rapid precession of the alpha states for the pheophytin radical and thus more efficiently form the molecular triplet (as illustrated in Figure 4). The action of $\Delta g \beta B_0 + I_Z N_Z$ breaks symmetry, resulting in an excess α nuclear spin states in the RP singlet state; triplet decay kinetics remove the β states from the radical pair. During time window (3), if coherent mixing of the electrons and the nucleus occurs, involving only the radical pair states, then excess beta states associated with the radical pair will be converted to alpha states. This net conversion is the novel feature in our proposed mechanism. The analogous process converting ^{3}PHβ_N to ^{1}PHα_N is not as strong because ^{3}PH is depleted to ^{3}P. During time window (4) excess alpha polarization is associated with the molecular triplet and excess beta polarization will be associated with the ground state: time resolved experiments could be used to detect this spin sorted state, and relaxation of the nuclei associated with the molecular triplet species could lead to net polarization. These two effects are distinct from our new mechanism, but are the essence of the RPM in cyclic reactions; this mechanism was simulated for our case in a previous publication, and failed to explain the polarization for the pheophytin acceptor.

Photoinduced Nuclear Polarization

J. Phys. Chem. B, Vol. 103, No. 3, 1999 **537**

represent the states of the fictitious electron spin.[7] The 16 basis set product operators are analogous to the product operators for any two-spin $^1/_2$ system; their form can be found elsewhere.[26] The following basis set operators were used for calculating the nuclear polarization: the singlet projection operator $\hat{\mathbf{P}}^s$, the triplet projection operator $\hat{\mathbf{P}}^t$, and two electron−nuclear product operators $(\hat{\mathbf{P}}^s\hat{\mathbf{N}}^z)$ and $(\hat{\mathbf{P}}^t\hat{\mathbf{N}}^z)$, describing the observable nuclear magnetization:

$$\hat{\mathbf{P}}^s = {}^1/_2(\hat{\mathbf{S}}^1 - \hat{\mathbf{S}}^x)\mathbf{N}^1 \tag{2}$$

$$\hat{\mathbf{P}}^t = {}^1/_2(\hat{\mathbf{S}}^1 + \hat{\mathbf{S}}^x)\mathbf{N}^1 \tag{3}$$

$$(\hat{\mathbf{P}}^s\hat{\mathbf{N}}^z) = {}^1/_2(\hat{\mathbf{S}}^1 - \hat{\mathbf{S}}^x)(\hat{\mathbf{N}}^\alpha - \hat{\mathbf{N}}^\beta) \tag{4}$$

$$(\hat{\mathbf{P}}^t\hat{\mathbf{N}}^z) = {}^1/_2(\hat{\mathbf{S}}^1 + \hat{\mathbf{S}}^x)(\hat{\mathbf{N}}^\alpha - \hat{\mathbf{N}}^\beta) \tag{5}$$

To obtain a homogeneous system of differential equations, we transformed the SLE into the superoperator format.[23] Alternatively, we could have solved the equations of motion using finite time step methods and/or Taylors expansion (Baker−Hausdorff) methods, but we found the SLE to be more efficient. Boxer and Goldstein previously solved a very similar problem analytically for the triplet yield assuming a truncated hyperfine interaction.[27] We retained a full dipolar interaction and had to use a correspondingly larger basis set; furthermore, we intended to study trajectories rather than simply obtain the triplet yields. For all these reasons, we used numerical methods. The coherent evolution assumed a Hamiltonian of the form indicated in Chart 1. In the Results section we contrast cases with the *C* and *D* terms from the hyperfine interaction to cases in which those terms were omitted (i.e., a truncated Hamiltonian). When the *C* and *D* terms are omitted the Hamiltonian as well as the initial state are block diagonal, and so the trajectory is guaranteed to conserve nuclear polarization. This corresponds to the case typically assumed in the previous solution phase radical pair mechanism calculations[28] and to the case assumed for the photosynthetic reaction center by Goldstein and Boxer.[27] Due to the fact that the (inverse of the) lifetime of the paramagnetic states is of the same order of magnitude as the hyperfine couplings, which in turn are of the same order of magnitude as the nuclear Zeeman coupling, this truncation of the nuclear raising and lowering operators is not valid. Therefore, for our calculations, we include the *C* and *D* terms, which were evaluated for each orientation as described below.

In superoperator notation,[29] the SLE assumes the following form:

$$\frac{d\hat{\rho}'(t)}{dt} = (-i/\hbar\hat{\hat{\mathbf{L}}} + \hat{\hat{\mathbf{K}}})\hat{\rho}'(t) \tag{6}$$

where $\hat{\hat{\mathbf{L}}}$ is the Liouville superoperator describing coherent evolution under the influence of the Zeeman and hyperfine interactions, $\hat{\hat{\mathbf{K}}}$ is the kinetic matrix describing back electron transfer, and $\rho'(t)$ is the transformed density operator. In the superoperator notation, $\rho'(t)$ is a 1×16 column vector, while $\hat{\hat{\mathbf{L}}}$ and $\hat{\hat{\mathbf{K}}}$ are 16×16 matrixes. The nuclear and electron spin operators are written as 16×1 row vectors (bras) or 1×16 column vectors (kets). In Liouville space, the expectation value of an observable operator is found by taking the dot product of this operator (bra) with the density operator (ket); it corresponds to calculating the trace of the dot product of this observable operator with the density matrix in Hilbert space. The matrix elements of the Liouville operator $\hat{\hat{\mathbf{L}}}$ and the kinetic matrix $\hat{\hat{\mathbf{L}}}$ are defined according to[23]

$$L_{ij,kl} = H_{ik}\delta_{jl} - H_{lj}\delta_{ik} \tag{7}$$

$$K_{ij,kl} = -{}^1/_2k_s[P^s_{ik}\delta_{jl} + P^s_{lj}\delta_{ik}] - {}^1/_2k_t[P^t_{ik}\delta_{jl} + P^t_{lj}\delta_{ik}] \tag{8}$$

The solutions of the SLE are $\rho(t) = \mathbf{U}\exp(\Lambda t)\mathbf{U}^{-1}\rho(0)$, where Λ is the eigenvalue matrix of the combined Liouville kinetic matrix $(-i/\hbar\hat{\hat{\mathbf{L}}} + \hat{\hat{\mathbf{K}}})$, and $\mathbf{U}$ is the unitary transformation that diagonalizes this matrix. The solutions were found numerically by diagonalizing and exponentiating the Liouville kinetic matrix for discrete values of time.

Nuclear polarization in the biradical states is associated with the electron−nuclear coherences represented by $\hat{\mathbf{P}}^s$, $\hat{\mathbf{P}}^t$, $(\hat{\mathbf{P}}^s\hat{\mathbf{N}}^z)$, and $(\hat{\mathbf{P}}^t\hat{\mathbf{N}}^z)$, whose time trajectories we calculated. Accumulation of the molecular triplet and ground states from the biradical states assumed to follow a first-order process. Therefore, the quantum yields of particular electron−nuclear coherences accumulated in the molecular triplet or the ground state can be calculated as the time integrals of the trajectory of these coherences:

$$\phi_{\mathbf{P}^t} = k_t\int_0^\infty \hat{\mathbf{P}}^t\cdot\hat{\rho}(t)dt \tag{9}$$

$$\phi_{\mathbf{P}^s} = k_s\int_0^\infty \hat{\mathbf{P}}^s\cdot\hat{\rho}(t)dt \tag{10}$$

$$\phi_{\mathbf{P}^t\mathbf{N}^z} = k_t\int_0^\infty (\hat{\mathbf{P}}^t \otimes \hat{\mathbf{N}}^z)\cdot\hat{\rho}(t)dt \tag{11}$$

$$\phi_{\mathbf{P}^s\mathbf{N}^z} = k_s\int_0^\infty (\hat{\mathbf{P}}^s \otimes \hat{\mathbf{N}}^z)\cdot\hat{\rho}(t)dt \tag{12}$$

Net nuclear polarization in the ground state is acquired if the quantum yields of the molecular triplet and the ground state singlet, $\phi_{\mathbf{P}^t\mathbf{N}^z}$ and $\phi_{\mathbf{P}^s\mathbf{N}^z}$, generated due to the coherent mixing and chemical kinteics, are not equal in magnitude and opposite in sign. This takes place in the presence of the *C* and *D* terms of the mixing Hamiltonian, as discussed in detail in the Results section, and is the centerpiece of the proposed mechanism.

Nuclear polarization in the molecular triplet and the ground singlet states are associated with the quantum yields $\phi_{\mathbf{P}^t\mathbf{N}^z}$ and $\phi_{\mathbf{P}^s\mathbf{N}^z}$. The trajectories of the nuclear coherences in the molecular triplet and the ground singlet states were calculated for discrete time points by numerical integrations of the corresponding electron−nuclear coherences in the biradical states:

$$(\hat{P}^t\hat{N}^z)_{gnd}(t) = \phi_{\mathbf{P}^t\mathbf{N}^z}(t) = k_t\int_0^t \hat{\mathbf{P}}^t\hat{\mathbf{N}}^z(t)dt \tag{13}$$

$$(\hat{P}^s\hat{N}^z)_{gnd}(t) = \phi_{\mathbf{P}^s\mathbf{N}^z}(t) = k_s\int_0^t \hat{\mathbf{P}}^s\hat{\mathbf{N}}^z(t)dt \tag{14}$$

Trajectories were computed using typical coupling strengths to assess the numerical stabilities and the typical range of parameters over which polarizations could be developed, before attempting to compute trajectories for specific orientations of the reaction center (vide infra). Time trajectories and quantum yields were computed using a time step of 60 ps and a maximum evolution time of 120 ns (2000 discrete time points). The required numerical precision was of the order of 10^{-6} (the

Photoinduced Nuclear Polarization

J. Phys. Chem. B, Vol. 103, No. 3, 1999 **539**

TABLE 1: Magnitudes and Orientations of the Anisotropic Interactions, and Kinetic Constants Used in the Simulations (Unless otherwise Indicated)

Anisotropic Tensorial Interactions

parameter, ref	constant	tensor components in the PAS			Euler angles for PAS→MFF transformation		
		xx	*yy*	*zz*	α'	β'	γ'
g-anisotropy tensor of BChl[30,31]	g_{BChl}	2.00329	2.00239	2.00203	0.4	1.88	−0.53
g-anisotropy tensor of BPheo[34]	g_{BPheo}	2.0038	2.0038	2.0029	0	0	0
hyperfine anisotropy tensor of BPheo[a]	A_{BPheo}	5 MHz	5 MHz	−10 MHz	0	0	0

Kinetic Constants

parameter	constant	value, s^{-1}	ref
light excitation	k_e	50	calcd from measured power (1−5 mW)
^{3}PH decay rate	k_{isc}	10^4	36
charge recombination from $^3(P^{+\bullet}H^{-\bullet})$ to ^{3}PH	k_t	5×10^8	40
charge recombination from $^1(P^{+\bullet}H^{-\bullet})$ to ^{1}PH	k_s	5×10^7	40
nuclear spin relaxation in the ^{3}PH state	$1/T_1'$	0.1−1	empirical
nuclear spin relaxation in the ^{1}PH state	$1/T_1$	0.1	empirical

[a] Estimated based on the isotropic Hyperfine constant,[41] assuming an axial tensor.

Boltzmann polarization is of the order of 6×10^{-6}) and was only possible with time steps less than 500 ps. The total length of the time trajectories was determined based on the slowest decaying trajectories, which arise for the orientations with the largest nuclear polarizations, and typically 100 ns is more than enough. Numerical stability was confirmed by verifying the normalization condition: $\phi_{\hat{P}^s} + \phi_{\hat{P}^t} = 1$ (i.e., conservation of the total number of molecules as product species). We also assessed the numerical precision by constructing "control" cases for which the final polarization of the singlet ground state and the molecular triplet state might be large, but would be expected to be equal and opposite, involving truncated hyperfine Hamiltonians, balanced singlet and triplet decay rates, and cases with either very large or very small *g* value differences, or with very large or very small nuclear Zeeman splittings, so that the dynamics have the effect of truncating the Hamiltonian.

Calculations of Trajectories for Particular Molecular Orientations Using the Full Anisotropic Expression for the Hamiltonian. The *g* values, the hyperfine couplings, and the chemical shifts are significantly anisotropic and the extent of polarization can range from negligible to substantial and even acquire either positive or negative values depending on the orientation. Therefore a full powder average needed to be considered. The **g**-anisotropy tensor and the hyperfine anisotropy tensor for P$^{\bullet+}$ were reported previously.[30−33] In the principal axes system (PAS), the tensor assumes the following values and orientations: $g_{zz} = 2.00203$ and is almost perpendicular to the π plane of the dimer (the angle between the plane normal and the *zz*-component is 22°), $g_{yy} = 2.00239$ and is very close to the local C_2 symmetry axis of the dimer, $g_{xx} = 2.00329$ and is roughly orthogonal to the *yy* component. The isotropic values for the **g** tensor and the hyperfine tensor of H$_L^{\bullet-}$ have been reported.[34,35] The **g**-tensor anisotropy of H$_L^-$ has not been described in the literature to the best of our knowledge and was assumed to be about 0.001 with its unique axis being perpendicular to the π plane. The anisotropy of the hyperfine tensor is of the order of two thirds of the coupling strength, and the unique axis is perpendicular to the π plane. The principal values and the orientations of the **g** and **A** tensors for P$^{\bullet+}$ and H$_L^{\bullet-}$ are entered in Table 1. The expressions for these interactions in the laboratory frame were generated according to the following. First, each of the interactions was expressed in the PAS. Subsequently, the tensors were rotated into the common "crystal fixed" frame (CFF), chosen to be the PAS of the **g** and the hyperfine anisotropy tensors of H$^{\bullet-}$, which coincide. Thus,

only the **g** tensor for P$^{\bullet+}$ needs to be rotated from its PAS into the CFF:

$$\tilde{\mathbf{g}}_{P^{\bullet+}}^{\mathbf{CFF}} = \mathbf{R}(\alpha',\beta',\gamma')\cdot\tilde{\mathbf{g}}_{P^{\bullet+}}^{\mathbf{PAS}}\cdot\mathbf{R}^{-1}(\alpha',\beta',\gamma') \quad (15)$$

where α', β', and γ' are the Euler angles describing the relative orientations of the PAS and the CFF of the P$^{\bullet+}$ **g** tensor, and **R** and **R^{-1}** are the rotation matrix and its inverse.

Then, the zero-quantum **g** tensor $\Delta\tilde{\mathbf{g}}^{\mathbf{PAS}} = \tilde{\mathbf{g}}_{H^{\bullet-}}^{\mathbf{CFF}} - \tilde{\mathbf{g}}_{P^{\bullet+}}^{\mathbf{CFF}}$ and the hyperfine tensor of H$_L^-$ were transformed into the rotor fixed frame (RFF):

$$\Delta\tilde{\mathbf{g}}^{\mathbf{RFF}} = \mathbf{R}(\alpha,\beta,\gamma)\cdot\Delta\tilde{\mathbf{g}}^{\mathbf{CFF}}\cdot\mathbf{R}^{-1}(\alpha,\beta,\gamma) \quad (16)$$

$$\tilde{\mathbf{A}}^{\mathbf{RFF}} = \mathbf{R}(\alpha,\beta,\gamma)\cdot\tilde{\mathbf{A}}^{\mathbf{CFF}}\cdot\mathbf{R}^{-1}(\alpha,\beta,\gamma) \quad (17)$$

The Euler angles, α, β, and γ represent molecular orientations with respect to the RFF. The molecules in a powder sample can assume any orientation. In our calculation, the orientational space was sampled by selecting 2500 random orientations.

The final rotation brings the Δ**g** and **A** tensors from the rotor frame to the laboratory fixed frame (LFF). The coherent mixing resulting in generation of nuclear magnetization, occurs on a nanosecond time scale, much faster than the sample rotation, and therefore, we disregarded the time dependencies of the mixing Hamiltonian introduced by the magic angle spinning, and the rotation to the LFF simply took form:

$$\Delta\tilde{\mathbf{g}}^{\mathbf{LFF}} = \mathbf{R}(0,\theta,0)\cdot\Delta\tilde{\mathbf{g}}^{\mathbf{RFF}}\cdot\mathbf{R}^{-1}(0,\theta,0) \quad (18)$$

$$\tilde{\mathbf{A}}^{\mathbf{LFF}} = \mathbf{R}(0,\theta,0)\cdot\tilde{\mathbf{A}}^{\mathbf{RFF}}\cdot\mathbf{R}^{-1}(0,\theta,0) \quad (19)$$

where θ is the magic angle (0.955 rad).

The final expressions for the terms of the mixing Hamiltonian in the LFF were calculated as

$$\omega_e = (\Delta\tilde{g}^{\mathbf{LFF}}(\alpha,\beta,\gamma))_{33} \quad (20)$$

$$A = (\tilde{A}^{\mathbf{LFF}}(\alpha,\beta,\gamma))_{33} \quad (21)$$

$$C = (\tilde{A}^{\mathbf{LFF}}(\alpha,\beta,\gamma))_{13} + i(\tilde{A}^{\mathbf{LFF}}(\alpha,\beta,\gamma))_{23} \quad (22)$$

$$D = (\tilde{A}^{\mathbf{LFF}}(\alpha,\beta,\gamma))_{13} - i(\tilde{A}^{\mathbf{LFF}}(\alpha,\beta,\gamma))_{23} \quad (23)$$

The ω_e, A, C, and D terms were calculated for 2500 orientations

540 *J. Phys. Chem. B, Vol. 103, No. 3, 1999*

Polenova and McDermott

(whose Euler angles were selected using the *Mathematica* built-in random number generator).

Calculations of the Steady-State Nuclear Polarizations and the Nuclear Polarization Buildup Curves. The steady-state nuclear polarizations were calculated according to the following kinetic Scheme 1:

SCHEME 1: Kinetic Scheme Used to Describe the Steady-State Accumulation of Nuclear Polarization
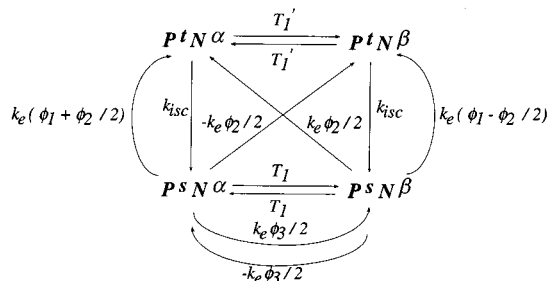
The scheme depicts the interconversion pathways between the singlet and the triplet electronic species for the nuclear α and β states. T_1 and T_1' are the nuclear spin−lattice relaxation rate constants of the ground (diamagnetic) and the excited (paramagnetic) states. k_{isc} is the rate constant of the triplet decay; ϕ_1, ϕ_2, and ϕ_3 are the quantum yields of $\hat{P}^t$, $\hat{P}^t\hat{N}^z$, and $\hat{P}^s\hat{N}^z$, respectively (eqs 9, 11, and 12); k_e is the light excitation rate constant. k_{isc} is known from the previous literature;[36] the rate constants describing the nuclear spin−lattice relaxation of the diamagnetic and the paramagnetic states, as well as the light excitation rate constant, were estimated as described previously.[4] The single-photon quantum yields of the various electron−nuclear coherences were calculated as described in the previous section.

The nuclear polarization buildup curves were calculated by solving the system of differential equations $d/dt\mathbf{M}(t) = \mathbf{K}\cdot\mathbf{M}(t)$ which can be written in matrix form:

$$\frac{\mathrm{d}}{\mathrm{d}t}\mathbf{M}(t) = W\cdot\mathbf{M}(t) \tag{24a}$$

$$\mathbf{M}(t) = ([\mathbf{P}^sN^\alpha](t), [\mathbf{P}^tN^\alpha](t), [\mathbf{P}^sN^\beta](t), [\mathbf{P}^tN^\beta](t)) \tag{24b}$$

$$W =$$

$$\begin{pmatrix} -k_e(\phi_1+\phi_3')-\frac{1}{T_1} & k_{isc} & k_e\phi_3''+\frac{1}{T_1} & 0 \\ k_e(\phi_1-\phi_2') & -k_{isc}-\frac{1}{T_1'} & k_e\phi_2'' & \frac{1}{T_1'} \\ k_e\phi_3'+\frac{1}{T_1} & 0 & -k_e(\phi_1+\phi_3'')-\frac{1}{T_1} & k_{isc} \\ k_e\phi_2' & \frac{1}{T_1'} & k_e(\phi_1-\phi_2'') & -k_{isc}-\frac{1}{T_1'} \end{pmatrix}$$

$$\tag{24c}$$

The kinetic constants describing quantum yields of $\hat{P}^t\hat{N}^z$ and $\hat{P}^s\hat{N}^z$ from the SLE trajectories, ϕ_2 and ϕ_3, were rewritten in terms of four new variables: $\phi_2' = {}^1/_2(|\phi_2|-\phi_2)$, $\phi_2'' = {}^1/_2(|\phi_2|+\phi_2)$, $\phi_3' = {}^1/_2(|\phi_3|-\phi_3)$, and $\phi_3'' = {}^1/_2(|\phi_3|+\phi_3)$, which were constrained to be positive, to ensure normalization of total nuclear states. The differential equations were solved numerically by diagonalizing and exponentiating the rate matrix; the final solution was obtained in the form $\mathbf{M}(t) = \exp(\mathbf{K}t)\mathbf{M}(0) = \mathbf{U}\cdot exp(\Lambda t)\cdot\mathbf{U}^{-1}\mathbf{M}(0)$. $\mathbf{M}(0)$ is a column vector of initial populations of each of the electron−nuclear coherences,

$$\mathbf{M}(0) = \begin{pmatrix} 0.5 \\ 0 \\ 0.5 \\ 0 \end{pmatrix}$$

and assumes the Boltzmann polarization for the initial $\mathbf{P}^s\mathbf{N}^\alpha$ and $\mathbf{P}^s\mathbf{N}^\beta$ states. $\mathbf{U}$ and $\mathbf{U}^{-1}$ are the unitary transformation that diagonalizes the $\mathbf{K}$ matrix, and its inverse. The nuclear polarization, defined as the population difference $[\mathbf{P}^s\mathbf{N}^\beta] - [\mathbf{P}^s\mathbf{N}^\alpha]$, was obtained from the corresponding elements of the $\mathbf{M}(t)$. The form of the kinetic matrix is similar to the kinetic matrix used for the calculations of the nuclear polarization according to the radical pair mechanism;[4] the difference between the two is only in the expressions for the quantum yields of the species participating in the mechanisms.

The anisotropic steady-state nuclear polarizations were computed for the 2500 orientations by using the single-photon quantum yields obtained previously and calculating $[\mathbf{P}^s\mathbf{N}^\beta] - [\mathbf{P}^s\mathbf{N}^\alpha]$ at the time of 2000 s. The time of approach to steady-state never exceeds 50 s. The final polarizations for the ground state species were stored in table form (containing the Euler angles describing the orientations CFF with regard to the RFF, anisotropic frequences for each particular orientations, and the corresponding quantum yields of the electron−nuclear coherences (eqs 9−12)) and used subsequently for computing the powder patterns and the MAS spectra.

The dependencies of the steady-state nuclear polarizations on the rate constants k_e, T_1, and T_1' were calculated for a single orientation that resulted in one of the largest steady-state polarizations for discrete values of the corresponding rate constant by fixing the rest of the kinetic constants in the scheme, at the time of 2000 s. The T_1 and T_1' dependencies were run for 2000 points each with the step of 0.002 s^{-1}; the k_e dependence was calculated for 500 discrete values of k_e with the step of 2 s^{-1}.

Calculations of the MAS Spectra. The MAS spectra of the thermally (Boltzmann) polarized powder patterns were produced by calculating the intensities of the spinning sidebands according to[37,38]

$$I_N(\alpha,\beta,\gamma) = f^*(\gamma)e^{i\gamma N}F(\gamma') \tag{25}$$

where $I_N(\alpha,\beta,\gamma)$ is the intensity of the Nth spinning sideband (counting from the centerband, which corresponds to the isotropic chemical shift) for a single molecule ("crystallite"), whose orientation is described by the Euler angles α, β, and γ with regard to the rotor frame. The functions F and f are defined as follows:

$$f^*(\gamma) = e(-i/\omega_r)(C_1 \sin\gamma + 1/2C_2 \sin 2\gamma - S_1 \cos\gamma - 1/2S_2 \cos 2\gamma) \tag{26}$$

$$F(\gamma') = \frac{1}{2\pi}\int_0^{2\pi} e^{-i\gamma N}f(\gamma')d\gamma' \tag{27}$$

where

$$f(\gamma') = e(+i/\omega_r)(C_1 \sin\gamma' + 1/2C_2 \sin 2\gamma' - S_1 \cos\gamma' - 1/2S_2 \cos 2\gamma') \tag{28}$$

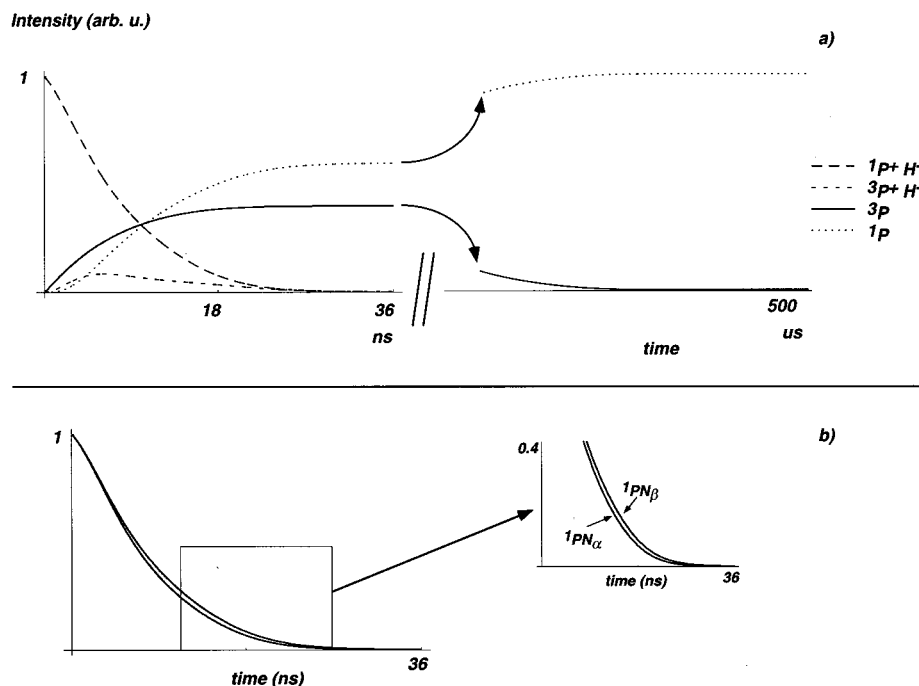and $\gamma' = \gamma + \omega_r t$, where ω_r is the rotor spinning speed.

Figure 2. The concentrations of the four chemical species: radical pair singlet $^1(P^{\bullet+} H^{\bullet-})$, radical pair triplet $^3(P^{\bullet+} H^{\bullet-})$, molecular triplet ^3P, and ground state P, are plotted as a function of time, as computed for the propagation of the radical pair states $^1(P^{\bullet+}H^{\bullet-})$ and $^3(P^{\bullet+}H^{\bullet-})$ with the Hamiltonian described in the text (Chart 1) with assumed coupling strengths of: $\Delta g = -2.06 \times 10^8$ Hz, $A = -3.42 \times 10^7$ Hz, $C = 1.22 \times 10^7 - i4.16 \times 10^7$ Hz, $D = 1.22 \times 10^7 + i4.16 \times 10^7$ Hz. The Euler angles describing this particular orientation are: $\alpha = 2.88$ rad, $\beta = 2.22$ rad, and $\gamma = 5.55$ rad. These orientations result in largest single turnover nuclear polarization. The decay kinetics of the photochemically formed singlet are clearly non exponential due to pronounced effects of the coherent mixing, as pointed out by Goldstein and Boxer.[27] The trajectories of the molecular triplet and the ground state were calculated as described in the text (eqs 13 and 14). On a much longer time scale the molecular triplet would decay to form the ground state as illustrated in Figure 1; a broken scale is indicated with the final populations shown. These longer (microsecond) time scales are not described in this model; they can be treated in a separate case due to the separation of the time scales. For the singlet radical pair species two curves are shown to illustrate the subtle difference in precession for a nucleus assumed to be in an α vs a β state.

CHART 1:　The Hamiltonian Used to Describe Coherent Dynamics[a]

$$\hat{H} = \begin{pmatrix} \hat{\omega}_n + \omega_e + A/4 & 0 & -C & 0 \\ 0 & \omega_n - \omega_e - A/4 & 0 & C \\ D & 0 & -\omega_n + \omega_e - A/4 & 0 \\ 0 & -D & 0 & \omega_n - \omega_e + A/4 \end{pmatrix}$$

$$\hat{H}_{tot} = \omega_n \cdot \hat{N}_z + \omega_e \cdot \hat{S}_z + A \cdot \hat{S}_z \hat{N}_z + C(\hat{S}_z \hat{N}_+ + \hat{S}_+ \hat{N}_z) + D(\hat{S}_z \hat{N}_- + \hat{S}_- \hat{N}_z)$$

[a] The Hamiltonian was combined with stochastic terms describing the fact that both singlets and triplets are drained by back electron transfer in the stochastic Liouville equation, utilizing an assumed initial state of unpolarized nucleus and a singlet electronic species. The Hamiltonian used previously by Boxer et al. and Kaptein et al. are similar except that truncation of the C and D terms led to a block-diagonal form.

The coefficients C_1, C_2, S_1, and S_2 are[38]

$$C_1(\alpha,\beta) = -\delta \frac{\sqrt{2}}{2} \sin 2\beta \left(1 + \frac{1}{3}\eta \cos 2\alpha\right) \quad (29)$$

$$C_2(\alpha,\beta) = \delta\left\{\frac{1}{2} \sin^2 \beta - \frac{1}{6}\eta(1 + \cos^2 \beta) \cos 2\alpha\right\} \quad (30)$$

$$S_1(\alpha,\beta) = \delta\eta\frac{\sqrt{2}}{3} \sin \beta \sin 2\alpha \quad (31)$$

$$S_2(\alpha,\beta) = \delta\eta\frac{1}{3} \cos \beta \sin 2\alpha \quad (32)$$

where δ and η are the anisotropy and asymmetry parameter of the chemical shift tensor, respectively; $\delta = \sigma_{zz}$, and $\eta = (\sigma_{yy} - \sigma_{xx})/(\sigma_{zz})$, in the RFF representation of the tensor. Simpler expressions in terms of the PAS form of the tensor can be derived for the special case that the tensor is axial, which

happens to be an excellent approximation for all of the tensors used here, although we did not utilize this approximation.

The ^{15}N CSA tensor of bacteriopheophytin in the PAS is $\sigma_{xx} = 125$ ppm, $\sigma_{yy} = 125$ ppm, and $\sigma_{zz} = 575$ ppm. The powder average can be obtained by either integrating over the Euler angles, or equivalently, by discretely sampling a random set of orientations, and weighting the intensities by the Boltzmann (thermal) polarization factor (6×10^{-6} for ^{15}N nuclei at room temperature):

$$I_N = (6 \times 10^{-6})\frac{1}{8\pi^2}\int_0^{2\pi} d\alpha \int_0^\pi \sin \beta \, d\beta \int_0^{2\pi} d\gamma I_N(\alpha,\beta,\gamma) \quad (33)$$

$$I_N = (6 \times 10^{-6})\frac{1}{2}\sum_{\alpha,\beta,\gamma} \sin \beta I_N(\alpha,\beta,\gamma)\Delta\beta \quad (34)$$

The two methods (analytic integrations vs discrete sampling of our 300 crystallites) gave indistinguishable spectra for the thermally polarized case.
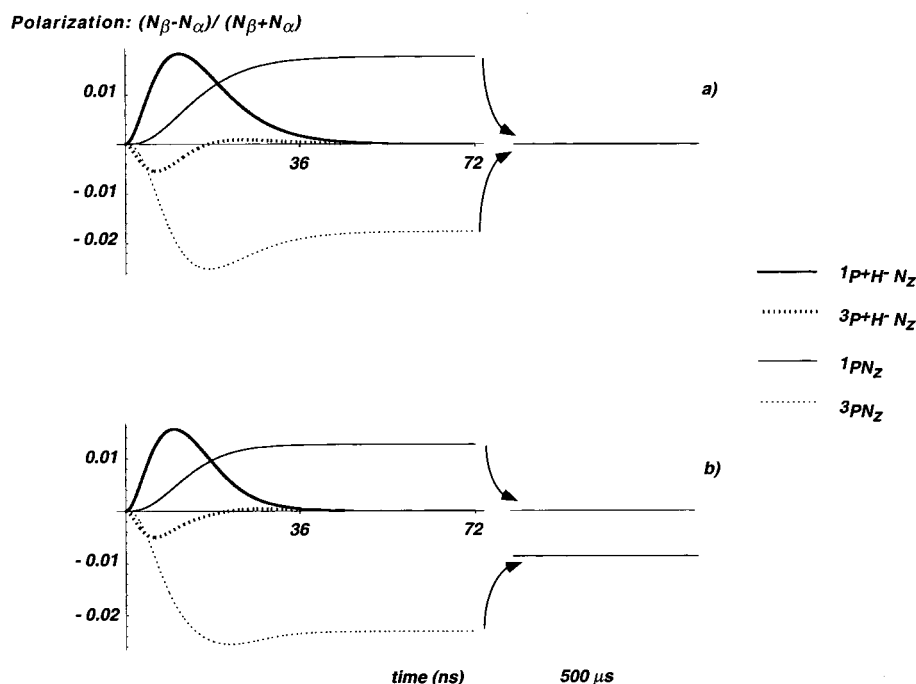
Figure 3. Difference in nuclear populations ($n_\beta - n_\alpha$) for an ^{15}N coupled to the pheophytin, using the same kinetic model as for Figure 2. The polarizations were obtained by calculating the time trajectories of the expectation values of the corresponding observable operators as explained in the text. These polarizations are plotted for all four chemical species ($^1(P^{\bullet+}H^{\bullet-})$, $^3(P^{\bullet+}H^{\bullet-})$, $^3(PH)$, $^1(PH)$). In the top part (a) the traces were computed with a truncated Hamiltonian ($\hat{P}^z\hat{N}^z$ dipolar hyperfine only) and below (b) the C and D terms were retained ($\hat{P}^z\hat{N}^+$ and $\hat{P}^z\hat{N}^-$) as explained in the text. The total polarization for very long times, when all of the molecular triplet has decayed, is indicated with broken time axis. For the top trace the net polarization (sum over all species) is zero at all times, although it is not zero for the ground state diamagnetic (NMR detectable) species except at the beginning and the end of the trace. If the polarization associated with the molecular triplet decays through spin−lattice relaxation on the microsecond timescale, then net polarization in the ground state species can be detected on a longer time scale, as described in Figure 1 caption. In the lower trace, with a more complete dipolar hyperfine Hamiltonian included, the net magnetization is not necessarily conserved, and the sum of all four polarization values is non zero except at the beginning of the evolution. For values typical for the photosynthetic reaction center (as described in Figure 2) the polarization yield for a single turnover is of the order of $10^{-4}-10^{-2}$. The largest effects are anticipated when Δg, A, C, and D are of similar order of magnitude, which occurs for orientations with minimum Δg (next to pheophytin plane). In Figure 1b stage 3 (5 ns), the nuclear raising and lowering operators have net action on radical pair manifold because N_+S_z and N_-S_z do not have equal weight. In the graph of polarization, 3b differs from 3a in that around 5 ns, the most strongly polarized radical pair state is $^1(P^{\bullet+}S^{\bullet-})$ with excess β nuclear spins. The term N_+S_z creates net excess α. While there is excess β in radical pair manifold, there is net excess α overall mostly in the molecular triplet ^{3}P which does not participate in the spin dynamics. Converting β to α with the N_+S_z term has the effect of reducing the β accumulated in ground state P, and increasing the α in ^{3}P so that they no longer are 50% each.

Discrete sampling of the same orientations was also performed for the calculation of the CIDNP polarized MAS spectra, except that the sideband intensities for each orientation (characterized by the Euler angles α, β, and γ in the rotor frame) were weighted by the corresponding steady-state polarizations $\Phi(\alpha,\beta,\gamma)$, calculated using the SLE as described above. The MAS spectra for the 300 crystallites were then coadded to form the MAS spectra

$$I_N = \frac{1}{2}\sum_{\alpha,\beta,\gamma} \Phi(\alpha,\beta,\gamma) \sin\beta I_N(\alpha,\beta,\gamma)\Delta\beta \quad (35)$$

Calculations of Anisotropic Static Powder Patterns. To calculate the static powder patterns for thermally and CIDNP polarized samples, the expressions for the ^{15}N resonance frequency as a function of molecular orientations in the LFF frame were constructed by applying a series of rotations to the CSA tensor and extracting the 3,3-element of the LFF representation (corresponding to a truncated or first-order Zeeman Hamiltonian):

$$\omega(\alpha,\beta,\gamma) = \tilde{\sigma}_{33}^{LFF} = (R^{LFF}(\phi,\theta,0)R^{RFF}(\alpha,\beta,\gamma)\tilde{\sigma}^{PAS} \cdot$$
$$(R^{RFF}(\alpha,\beta,\gamma))^{-1}(R^{LFF}(\phi,\theta,0))^{-1})_{33} \quad (36)$$

where $\tilde{\sigma}^{PAS}$ is the PAS representation of the CSA tensor.

$R^{RFF}(\alpha,\beta,\gamma)$ is the rotation matrix that transforms the PAS representation into the RFF (since the CFF coincides with PAS for this case); α, β, and γ are the Euler angles describing the orientations of the individual crystallites in the sample with respect to the RFF. $R^{LFF}(\phi,\theta,0)$ is the transformation from the RFF into the LFF representation; θ is the polar angle (the Magic angle, 0.955 rad), ϕ is the azimuthal angle. The powder patterns were calculated by generating the $\sin\beta$ weighted frequency histograms for the same selection of 300 crystallites. Later, another simulation was performed for a random selection of 2500 crystallites. The peak intensity of each crystallite was multiplied by the Boltzmann factor (6×10^{-6}). Convolution with a Gaussian line shape function was applied for smoothing; the homogeneous line width of the resonance peak of each individual crystallite was assumed to be 1 ppm, which is close to the line widths in the experimentally detected NMR spectra. For simulating the CIDNP polarized powder patterns, the resonance intensities of each individual crystallite were multiplied by their steady-state polarization yields. The thermally and CIDNP polarized powder patterns were calculated according to two different procedures. In the first set of simulations, ϕ (the azimuthal angle in the RFF to LFF transformation) was set to 0. In the second set of simulations, an additional averaging over ϕ was performed, namely, by making a table of ϕ values ranging from 0 to 2π with 20° steps, therefore

Photoinduced Nuclear Polarization

J. Phys. Chem. B, Vol. 103, No. 3, 1999 **543**

SCHEME 2: The Coordinate Systems Used in Describing the Anisotropic Interactions (Difference in *g* values, Hyperfine Couplings)[a]
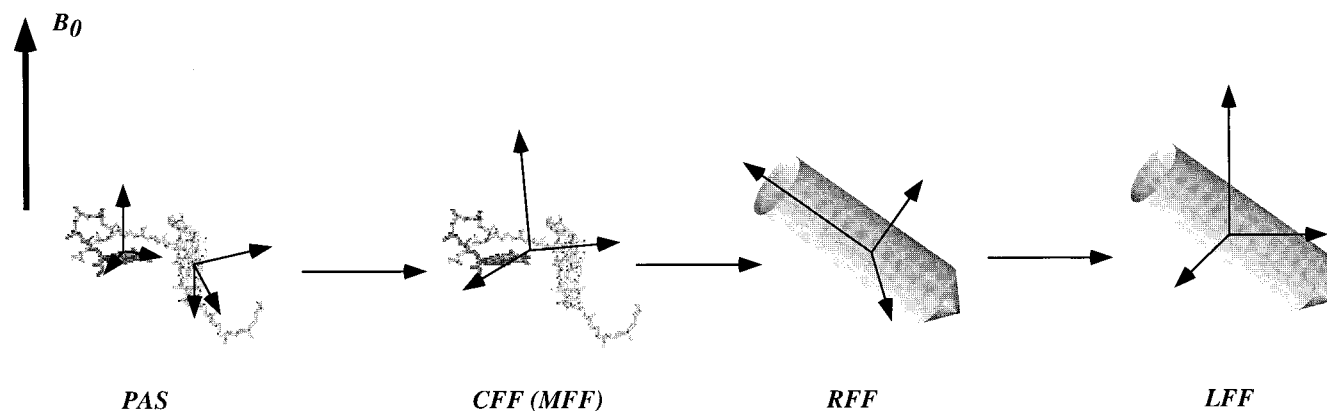
a The first cartoon shows the relative orientations of the PAS systems of the BChl dimer (lighter molecule) and BPheo (darker molecule). the PAS has to be rotated into the common reference frame (MFF); the MFF for BChl and BPheo is shown on the second cartoon. MFF of each molecular orientation has to be transformed into the rotor fixed frame (RFF) which is drawn on the third cartoon. The transformation between the MFF and the RFF is specified by Euler angles α, β, and γ, which were randomly chosen (a set of 300 Euler angles was generated) to represent different molecular orientations in the sample. The final transformation brings the RFF into the LFF; the LFF coordinates are shown on the fourth cartoon. The *z*-axis of the LFF is parallel to the magnetic field vector B_0 (shown on the left).
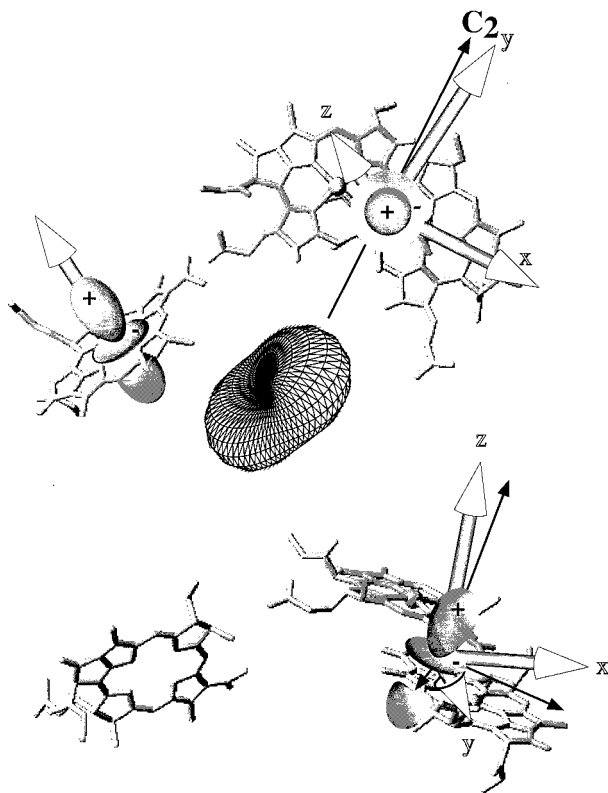

Figure 4. The molecular orientations of the tensor axes of significance to this problem are indicated on the molecule coordinates. The difference in *g* values, which causes the most significant singlet triplet mixing at 10 T, has its largest and smallest directions as indicated on the diagram. These physical directions are associated with nonzero *A*, *C*, and *D* terms in the dipolar Hamiltonian and give rise to the most significant net polarizations for single turnover conditions, since Δg, *A*, *C*, and *D* have similar order of magnitude values. In this region the dipolar coupling frequency (*A* term) for the pheophytin happens to be negative in sign (N_α precesses faster) and that for the bacteriochlorophyll donor happens to be positive (N_β precesses faster), as indicated.

generating a total of 5400 orientations from the original 300 crystallites. This angle describes the fact that the rotor acquires a random phase between the photon absorption and NMR detection. We note that the initial number of crystallites utilized
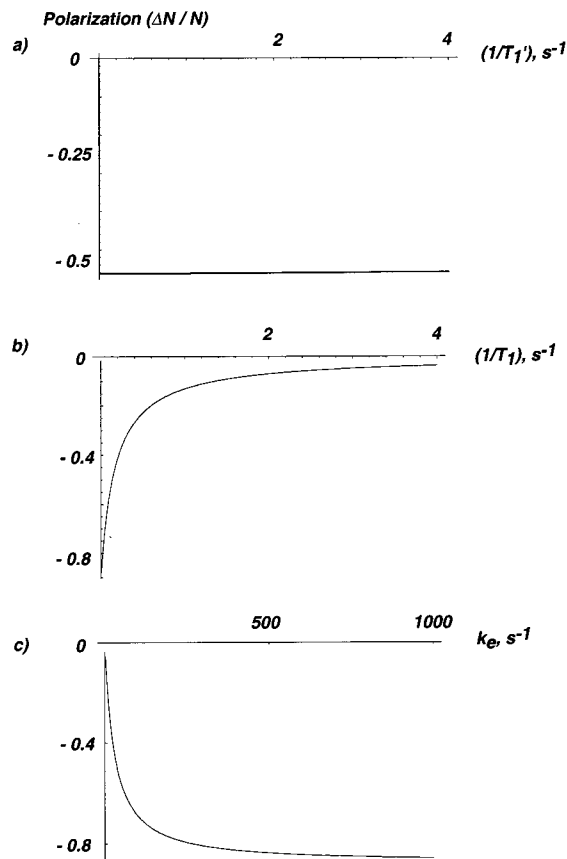

Figure 5. The steady-state nuclear polarization as a function of (a) nuclear relaxation rate constant in the molecular triplet $(1/T_1')$ (calculated assuming $k_e = 50$ s^{-1}, $(1/T_1) = 0.1$ s^{-1}, $k_{isc} = 10^4$ s^{-1}), (b) nuclear relaxation rate constant in the ground state $(1/T_1)$ (calculated assuming $k_e = 50$ s^{-1}, $(1/T_1') = 0.1$ s^{-1}, $k_{isc} = 10^4$ s^{-1}), (c) light excitation rate constant k_e (calculated assuming $(1/T_1') = 0.1$ s^{-1}, $(1/T_1) = 0.1$ s^{-1}, $k_{isc} = 10^4$ s^{-1}). The steady-state nuclear polarizations were calculated for discrete values of the rate constants by assuming fixed values for the rest of the kinetic constants (Scheme 2). The orientation with $\alpha = 3.26$ rad, $\beta = 2.29$ rad, $\gamma = 5.28$ rad which results in large negative polarization (emissive signals) was chosen.

(300) was too small to sample the powder pattern well (and the second set of 2500 crystallites was barely sufficient), but more
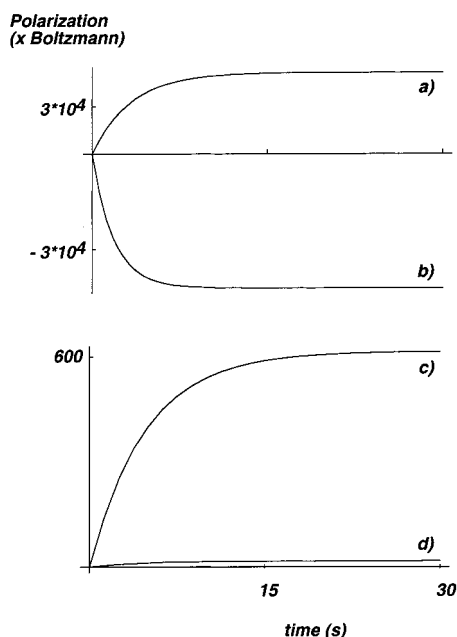
Figure 6. The approach of nuclear polarization to steady state is calculated according to the kinetic scheme (Scheme 1), with $k_e = 50$ s^{-1}, $T_1 = 10$ s, $T_1' = 1$s, $k_{isc} = 10^5$ s^{-1}. Curves a−d result from orientations giving rise to (a) large positive polarization (corresponding to $\alpha = 2.56$ rad, $\beta = 1.59$ rad, $\gamma = 5.36$ rad), (b) large negative polarization (corresponding to $\alpha = 3.26$ rad, $\beta = 2.29$ rad, $\gamma = 5.28$ rad), (c) intermediate polarizations (100−1000 times Boltzmann) (corresponding to $\alpha = 0.54$ rad, $\beta = 0.21$ rad, $\gamma = 0.61$ rad); (d) the smallest polarizations (1−100 times Boltzmann) (corresponding to $\alpha = 0.45$ rad, $\beta = 1.71$ rad, $\gamma = 1.70$ rad). The time of approach to steady state is of the order of 15 s for the largest polarizations, and 25 s for the intermediate and smallest polarizations.

than enough to compute a MAS spectrum (50 orientations is sufficient for generating a MAS spectrum), due to the additional averaging over the rotor phase.

Results and Discussion

We have calculated the trajectories of chemical concentrations of the radical pair singlet, radical pair triplet, molecular triplet and ground state species following a single photon absorption as shown in Figure 2a; we used the Hamiltonian described in Chart 1 with values for the coherent mixing terms and other kinetic constants mainly taken from previous literature and entered in Table 1. We used the SLE (eq 6) to produce the trajectories of the density matrix and of the amplitudes of the radical pair states $^1(P^{\bullet+}H^{\bullet-})$ and $^3(P^{\bullet+}H^{\bullet-})$. The ground state and molecular triplet species are derived through the integral expression for the back electron transfer reactants (eqs 9−12). It is of particular interest to predict whether $\phi_{P^sN^z} = -\phi_{P^iN^z}$ at long times: if these yields are unequal then net nuclear polarization N^z has resulted from the coherent evolution. As was indicated previously,[27] the kinetics of singlet decay are highly nonexponential due to the fact that the dominant process is coherent mixing to form the biradical triplet. The decay to first the radical pair triplet, then molecular triplet, and the ground state can be seen on the 10 ns time scales.

The effect of nuclear couplings on the mixing rates of the radical pair states is substantial as indicated in the two radical pair singlet decay curves for two nuclear states of a nearby ^{15}N (Figure 2b). This is the spin sorting phenomenon described previously by Kaptein et al. and Closs et al. (reviewed in ref 23) and is expected to be quite pronounced in this system based on these calculations. Between 0.5 and 3 ns, substantial
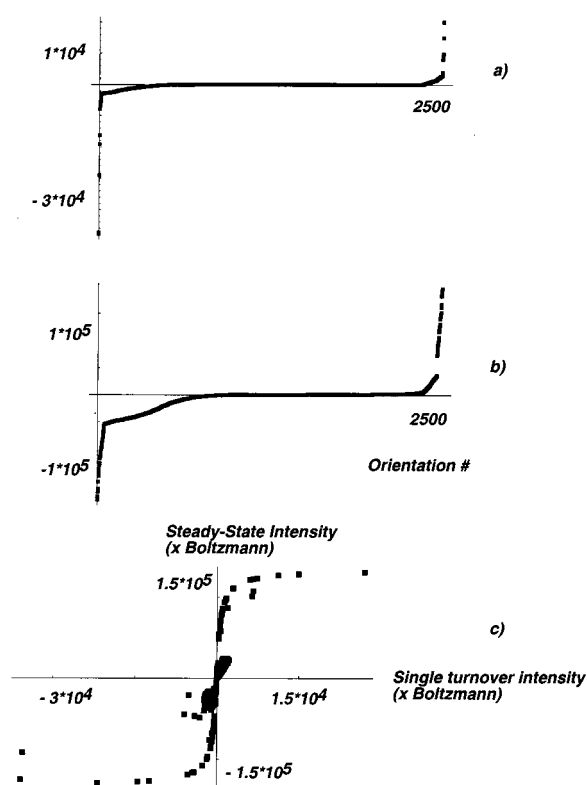

Figure 7. Histogram of the distribution of polarization intensities (both single turnover (a) and estimate steady state (b)). The steady-state polarization intensities are plotted to show the asymmetry in distribution of positive and negative polarizations, which gives rise to the total nonzero polarization. The correlation between single turnover and steady-state values (c) shows that the steady-state polarizations are not directly correlated to the single turnover rate, due to the fact that ϕ_{P^i} is also anisotropic and enters into the steady-state calculations (Chart 1).

polarization is associated with each of the four chemical species as illustrated in Figures 3a and b. We performed one control calculation without C and D terms and another with large C and D terms to illustrate the important effect of this part of the dipolar Hamiltonian. If a truncated dipolar Hamiltonian is used (Figure 3a), and electron−nuclear relaxation terms are omitted, then the sum of all four polarization values remains constant (zero) throughout our simulations. The two nuclear spin manifolds in this case can be described with separate Hamiltonians, and the product space is block diagonal with no electron terms connecting the two nuclear states. On the other hand, if the C and D terms are included (Figure 3b), then significant net polarization can be developed through the C and D terms. This polarization can be expected whenever the C and D terms are active on a spin system that is temporarily polarized so that net action for the raising and lowering operators can be expected. As can be seen from these plots, the combination of these kinetic factors acts to keep the net polarization in the radical pair manifold low, while the molecular triplet (draining out of the radical pair triplet) systematically accumulates a particular nuclear state.

The extent of polarization is greatest when Δg, A, C, and D and the triplet decay rate are of similar orders of magnitude. Due to the fact that $\Delta\mathbf{g}$ and the hyperfine terms are significantly anisotropic, the extent of polarization is anisotropic as well. Figure 4 illustrates the tensor orientations in the molecular frame and indicates the directions in which the largest effect might be expected (i.e., when Δg is smallest). The anisotropic effects are simulated in detail as described in the Materials and Methods section, the results of which are discussed below.
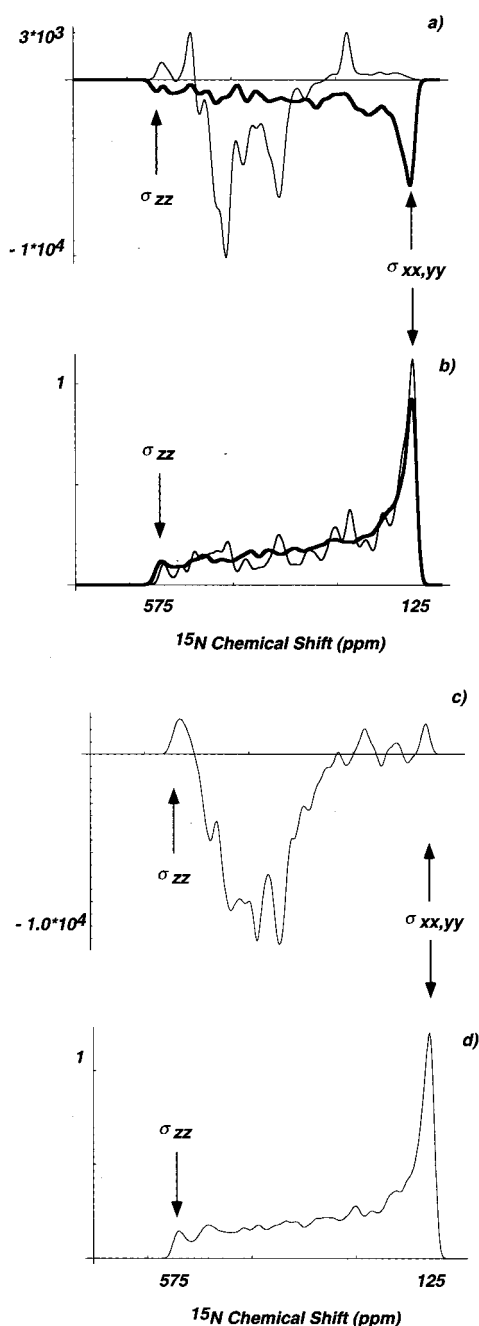
Figure 8. ^{15}N powder patterns for the BPheo acceptor calculated for the following cases: (a) CIDNP polarized, assuming fixed orientation of the molecules with respect to the rotor axis at the instance of detecting the NMR signal (light line) and assuming that averaging of molecular orientations around the rotor axis took place between light excitation and the NMR detection (heavy line); (b) thermally polarized, assuming static powder (light line), and with additional averaging around the rotor axis (heavy line); (c) CIDNP polarized, assuming fixed orientation of the molecules with respect to the rotor axis at the instance of detecting the NMR signal; (d) thermally polarized, assuming static powder. Spectra (a) and (b) were calculated for 300 orientations as described in the Materials and Methods section. To calculate the rotationally scrambled spectra, additional orientations were generated by generating a grid of values of ϕ (the polar angle describing the rotor axis) equally spaced by 20°, and assumed to carry the same intensity. The other Euler angles were kept invariant. Therefore, a total of 5400 orientations were generated from the original 300. Spectra (c) and (d) were generated for 2500 orientations as described in the Materials and Methods section.

The experiments were conducted with CW illumination and photoaccumulation, because the use of single saturating laser pulses has thus far been impossible, and because the long nuclear

spin lattice relaxation times for carbon and nitrogen make this photoaccumulation profitable. Therefore, to estimate the extent of steady state polarization and the time scale of approach to steady state we simulated kinetic competition between photo-excitation of polarization, spin−lattice relaxation in both the ground and the molecular triplet states, and intersystem crossing to relax the molecular triplet to the ground state. This simulation mirrors closely the simulations we previously performed for the radical pair mechanism,[4] and in fact embodies the mechanism for the radical pair for the trivial case in which the polarizations for the molecular triplet and the ground state are equal and opposite (i.e., truncated Hamiltonian). In this case substantial difference between the nuclear spin−lattice relaxation time for the ground electron state (T_1) and for the molecular triplet (T_1') are needed to achieve net polarization. In contrast, for the mechanism proposed herein, such a difference in the relaxation rates is not essential, and in fact, the relaxation in the molecular triplet state plays little or no role in the buildup of the steady-state nuclear polarization in the ground state (shown in Figure 5a). The relaxation rate of the nuclei in the ground state, on the other hand, is an important possible loss or "leakage factor", and the maximum polarization is generated for the nuclei with slow T_1 (Figure 5b). Typical relaxation rates of ^{15}N in solid state are of the order $0.1-1$ s^{-1} and appear to result in large steady-state polarizations, according to the calculations. The light excitation rate constant also contributes to the steady-state polarizations: for small excitation rates no or little polarization is predicted, while the polarization intensity reaches steady-state for larger excitation rates (Figure 5c).

The simulated time evolution of the polarization during approach to steady state shown in Figure 6 is in good qualitative agreement with the data reported previously[39] in terms of net enhancement (ca. 300−1000) and time scale (ca. 1−5 s). For these simulations we assumed that $T_1 = 10$ s, $T_1' = 1$ s, and $k_e = 50$ s^{-1}.

To simulate the NMR spectrum expected for the N-II and N-IV nitrogens of the pheophytin acceptor, we selected 2500 molecular orientations at random, computed the yields for the molecular triplet, the singlet, and the nuclear polarization associated with both. The problem of computing anisotropic coupling strengths involves a tedious series of coordinate systems, as illustrated in Scheme 2. The principal axes system (PAS) for each interaction is identified in terms of important local degrees of freedom (high-symmetry molecular axes, internuclear vectors, etc.) and is the axis system in which that interaction is diagonal. A crystal fixed frame (CFF) (or the molecular fixed frame, MFF) provides a coordinate system in which all the PAS can be described at once; each PAS should be fixed in definite spatial/angular relations through Euler rotations that take PAS to the common CFF. To construct a powder, the CFF is related to the rotor fixed frame using many randomly selected Euler angles (which describe the way in which the molecule was placed into the rotor). The rotor is finally related to laboratory fixed frame (LFF) with yet another set of Euler angles which are time dependent, to describe magic angle spinning. The interactions are often defined most conveniently in the LFF since the applied magnetic field and the spin operators in this frame have very simple expressssions. For each crystallite, we modeled the steady state polarization under the assumption of particular nuclear relaxation rates, photoexcitation rates, and intersystem crossing decay rates.

In practice we first constructed the interactions in the CFF, by determining both the PAS values and the orientations and defining the CFF in relation to the pheophytin coordinates. To
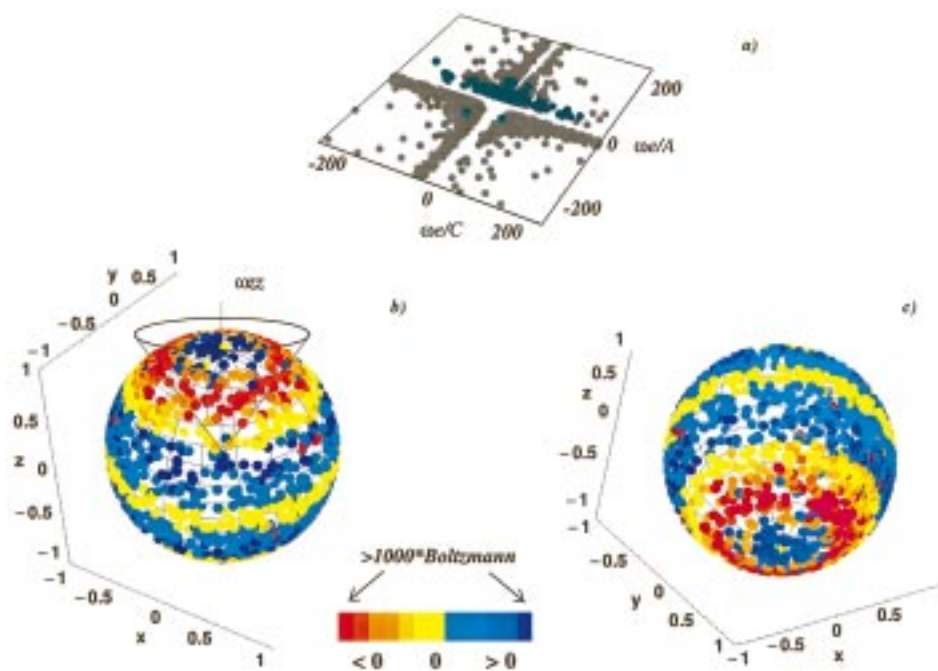
Figure 9. (a) Distribution of CIDNP steady-state polarization intensities is plotted vs ω_e/C and ω_e/A. Darker points on the graph correspond to the largest negative ($1 \times 10^4 - 3 \times 10^4$ times Boltzmann) polarizations, principally responsible for the ensemble averaged emissive NMR spectra. (b) Orientational distribution of CIDNP steady-state polarization intensities (top view). (c) Orientational distribution of CIDNP steady-state polarization intensities (bottom view). Polarization intensities are coded in color on a Cartesian sphere. The laboratory frame z-axis is in the vertical direction. Steady-state yields were calculated assuming $k_e = 50$ s^{-1}, $T_1 = 10$ s, $T_1' = 1$s, $k_{isc} = 10^5$ s^{-1}. The largest polarization belts in the laboratory frame result from the orientations which give rise to the closest match in the coupling constants: $\Delta\mathbf{g}$, A, C, and D terms.

begin the calculations for a particular crystallite, we specified that crystallite by randomly selecting the Euler angle values (α, β, and γ) describing the rotation of the CFF to the RFF. We then computed the corresponding tensorial interactions (both Δg values and the hyperfine interaction) in the laboratory frame assuming that the rotation from the RFF to the LFF had no azimuthal component, and evaluated the elements associated with the truncated g interaction, and the A, C, and D terms of the hyperfine interaction as described in the Materials and Methods section. These values were then utilized to perform a SLE trajectory, retaining the yields for the singlet, the triplet, and the polarizations associated with both species, and finally a steady-state polarization was computed. The polarization varied significantly among the crystallites (due to the anisotropy of interactions), as illustrated with our histograms of single turnover and steady-state polarizations in Figure 7.

The powder patterns and the MAS spectra were computed with and without a correction for the random accumulation of rotor phase between illumination and NMR excitation as described in the Materials and Methods section. The polarized static spectra are very anisotropic, and the strongest polarizations are associated with particular ranges of ratios of coupling strengths as emphasized in Figure 9a. These ratios occur in particular orientations of the sample as illustrated in Figure 9b and c. The orientation leading to the largest polarization is nearly, but not exactly, perpendicular to the pheophytin normal, and thus corresponds to nitrogens that resonate near the parallel edge of the axial CSA powder pattern (Figure 8). This is principally dictated by the fact that this is the orientation with the smallest g value difference and thus is subject to the maximal lifetime under the influence of the hyperfine interaction, and accumulates the largest effect of the hyperfine interaction before decaying to the molecular triplet. This orientation can be visualized using Figure 4 where the molecular structure and the anisotropic interactions are compared spatially. Introducing

the accumulation of random phase between the photon absorption and the NMR pulse had the effect of removing much of the anisotropy in the spectrum that would be expected for a strictly static sample, as illustrated by Figure 8. This observation strongly suggests that measurements of oriented samples would be of interest. The 300 orientations generated at first were not sufficient to obtain smooth powder patterns. We therefore ran an additional simulation for a random selection of 2500 orientations. The corresponding static thermal and CIDNP polarized powder patterns are shown in Figure 8c and d, respectively.

Using the Herzfeld−Berger algorithm, the MAS SSB pattern for each crystallite was also computed. Figure 10 (a and b) compares the MAS spectrum for the N-II and the N-IV nitrogens in the pheophytin acceptor species as computed for the steady state polarized spectrum and a simulated thermally polarized spectrum.

The relative orientations of the tensor axes in the crystal or molecular fixed frame are important for determining the final polarized spectra. As indicated by detailed EPR studies[30,31] the $\mathbf{g}$ tensor of the primary donor is aligned with its most shielded element roughly perpendicular to the macrocycles' normal (ca. 20°) and the least shielded element roughly orthogonal to the C_2 symmetry axis in the plane of the macrocycles, corresponding to the following Euler angles for the PAS→MFF transformation (MFF was chosen to be the PAS of the $\mathbf{g}$ tensor of the primary acceptor): $\alpha^{PAS \rightarrow MFF} = 0.4$, $\beta^{PAS \rightarrow MFF} = 1.88$, $\gamma^{PAS \rightarrow MFF} = -0.54$. The $\mathbf{g}$ tensor for the acceptor anion radical was assumed to have an axial shape and to have its most shielded (unique) element exactly perpendicular to the macrocycle (since data for this species is lacking). The dipolar hyperfine axes for both species were assumed to have their principal axes perpendicular to the aromatic plane of the heterocycle. Figure 10c illustrates the fact that if we deliberately misalign the dipolar and the $\mathbf{g}$ tensor axes we cannot achieve adequate agreement between the

Photoinduced Nuclear Polarization

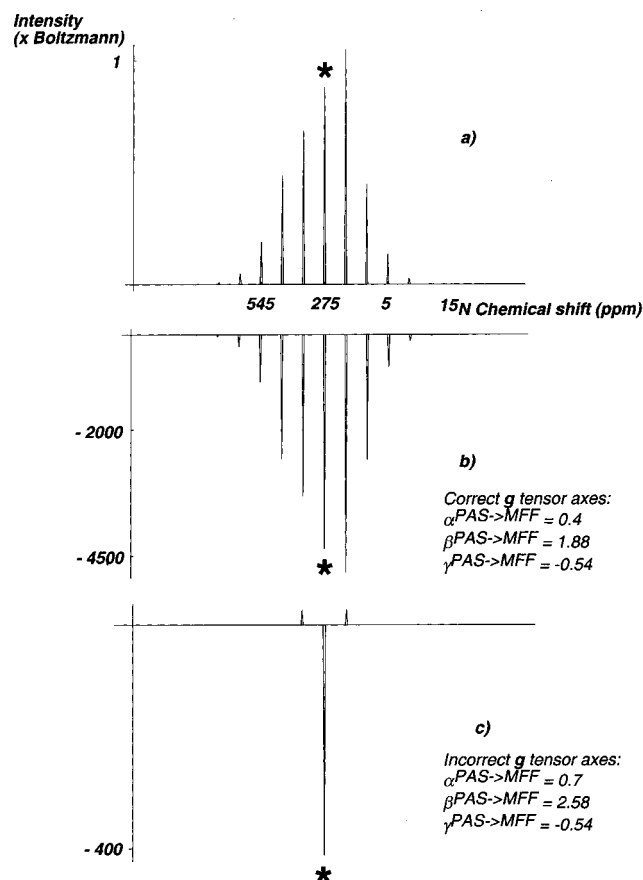*J. Phys. Chem. B, Vol. 103, No. 3, 1999* **547**

Figure 10. Simulated ^{15}N MAS spectra at 3.6 kHz of N-II and N-IV in BPheo assuming (a) thermally polarized sample, (b) CIDNP polarized sample, (c) CIDNP polarized sample with deliberately chosen incorrect BPheo **g** tensor orientation (described in the text). Correct orientations are given in Table 1. The spectra were computed by discrete sampling of the 300 orientations using the expressions for the sidebands' intensities as described in Materials and Methods section.

observed and the computed spectra: the computed spectra then exhibit far too much polarization with a different orientational distribution (not shown), and give rise to a distorted MAS spectrum. In this calculation it was assumed that the **g** tensor of the donor was orthogonal with respect to the **g** tensor of the acceptor, resulting in the following Euler angles: $\alpha^{PAS\rightarrow MFF} = 0.7$, $\beta^{PAS\rightarrow MFF} = 2.58$, $\gamma^{PAS\rightarrow MFF} = -0.54$. We also performed calculations assuming other orientations of the **g** tensor of the acceptor proposed in (31) and indistinguishable on the basis of the EPR data. The MAS spectra generated from these orientations are inconsistent with our experimental data. It would be very interesting to elucidate the requirements on the mutual tensor orientations that result in absorptive phaseable MAS spectrum; this question will be adressed elsewhere.

Conclusion

We propose a new mechanism for photoinduced nuclear polarization in reaction centers. Chemical kinetics cause the well-known phenomenon of spin sorting to result temporarily in large polarizations in the radical pair system. The action of the C and D terms of the dipolar hyperfine Hamiltonian converts this *temporary* polarization into net permanent polarization. For this coherent mechanism, no relaxation or cross-relaxation is needed in order to generate large nuclear polarizations. Simulations of the nuclear polarizations for Bpheo N-II and N-IV show good agreement with the data in terms of the sign and the order of magnitude of nuclear polarization, the time of the approach

to steady state, and the MAS pattern and the spinning sidebands intensities. Experiments are under way to test the specific predictions of the mechanism for reaction centers and to address other systems that may exhibit strong nuclear polarization under similar conditions.

Glossary

CIDNP	chemically induced dynamic nuclear polarization
NMR	nuclear magnetic resonance
P	special pair, primary electron donor
H	primary electron acceptor, pheophytin$_L$
Q	quinone
Q_{dep}	quinone-depleted
Q_{red}	quinone-reduced
Rb.	Rhodobacter
SSNMR	solid-state nuclear magnetic resonance
RPM	radical pair mechanism
BChl	Bacteriochlorophyll
BPheo	Bacteriopheophytin
SLE	stochastic Liouville equation
ODMR	optically detected magnetic resonance
DNP	dynamic nuclear polarization
PAS	principal axes system
CFF	crystal fixed frame
RFF	rotor fixed frame
MFF	molecular fixed frame
LFF	laboratory fixed frame

References and Notes

(1) Zysmilich, M. G.; McDermott, A. E. *J. Am. Chem. Soc.* **1994**, *116*, 8362−8363.

(2) Zysmilich, M. G.; McDermott, A. *J. Am. Chem. Soc.* **1996**, *118*, 5867−5873.

(3) Zysmilich, M. G.; McDermott, A. *Proc. Natl. Acad. Sci. U.S.A.* **1996**, *93*, 6857−6860.

(4) McDermott, A.; Zysmilich, M. G.; Polenova, T. *SSNMR* **1998**, *11*, 21−47.

(5) Closs, G. L. *J. Am. Chem. Soc.* **1969**, *91*, 4552−4554.

(6) Kaptein, R.; Oosterhoff, L. J. *Chem. Phys. Lett.* **1969**, *4*, 195−197.

(7) Abragam, A. *Principles of Nuclear Magnetism*, 10th ed.; Oxford University Press: Oxford, 1994; p 599.

(8) Wind, R. A.; Duijvestijn, M. J.; van der Lugt, C.; Maneschijn, A.; Vriend, J. *Prog. NMR Spectrosc.* **1985**, *17*, 33−67.

(9) Wind, R. A.; Lewis, R.; Lock, H. *Adv. Chem. Ser.* **1993**, *229*, 45.

(10) Maresch, G. G.; Kendrick, R. D.; Yannoni, C. S. *J. Magn. Res.* **1989**, *82*, 41.

(11) Un, S.; Prisner, T.; Weber, R. T.; Seaman, M. J.; Fishbein, K. W.; McDermott, A. E.; Singel, D. J.; Griffin, R. G. *Chem. Phys. Lett.* **1992**, *189*, 54−59.

(12) Afeworki, M.; Schaefer, J. *Macromolecules* **1992**, *25*, 4092−4096.

(13) Pines, A.; Long, H. W.; Crawford, G. P. *J. Phys. Chem.* **1995**, *99*, 11989.

(14) Suter, D.; Rosatzin, M.; Mlynek, J. *Phys. Rev. Lett.* **1991**, *67*, 34.

(15) Suter, D. *Phys. Rev. A* **1992**, *46*, 344.

(16) Buratto, S. K.; Shykind, D. N.; Weitekamp, D. P. *Phys. Rev.* **1991**, *44*, 9035.

(17) Tycko, R.; Reiner, J. A. *J. Phys. Chem.* **1996**, *100*, 13240.

(18) Burghaus, O.; Klein, M. P. *Chem. Phys. Lett.* **1995**, *243*, 486-492.

(19) Kothe, G.; Weber, S.; Ohmes, E.; Thurnauer, M. C.; Norris, J. R. *J. Phys. Chem.* **1994**, *98*, 2706−2712.

(20) Kothe, G.; Weber, S.; Ohmes, E.; Thurnauer, M. C.; Norris, J. R. *J. Am. Chem. Soc.* **1994**, *116*, 7729−7734.

(21) Jeschke, G.; Schweiger, A. *Mol. Phys.* **1996**, *88*, 355−383.

(22) Kubo, R. *Adv. Chem. Phys.* **1969**, *15*, 101−127.

(23) Hoff, A. J. *Quart. Rev. Biophys.* **1984**, *17*, 153−282.

(24) Boxer, S. G.; Chidsey, C. E. D.; Roelofs, M. G. *Proc. Natl. Acad. Sci. U.S.A.* **1982**, *79*, 4632−4636.

(25) Boxer, S. G.; Chidsey, C. E. D.; Roelofs, M. G. *Annu. Rev. Phys. Chem.* **1983**, *34*, 389−417.

(26) Jeschke, G. *J. Chem. Phys.* **1997**, *106*, 10072−10086.

(27) Goldstein, R. A.; Boxer, S. G. *Biophys. J.* **1987**, *51*, 937−946.

(28) Kaptein, R. In *Chemically Induced Magnetic Polarization*; Mussm L. T., Atkins, P. W., McLauchlanm K. A., Pederson, J. B., Eds.; D. Reidel: Dordrecht, The Netherlands: 1977.

(29) Jeener, J. *Adv. Magn. Res.* **1982**, *10*, 1−51.

(30) Prisner, T. F.; van der Est, A.; Bittl, R.; Lubitz, W.; Stehlik, D.; Möbius, K. *Chem. Phys.* **1995**, *194*, 361−370.

(31) Klette, R.; Törring, J. T.; Plato, M.; Möbius, K.; Bönigk, B.; Lubitz, W. *J. Phys. Chem.* **1993**, *97*, 2015−2020.

(32) Käss, H.; Rautter, J.; Bönigk, B.; Höfer, P.; Lubitz, W. *J. Phys. Chem.* **1995**, *99*, 436−448.

(33) Lendzian, F.; Huber, M.; Isaacson, R. A.; Endeward, B.; Plato, M.; Bönigk, B.; Möbius, K.; Lubitz, W.; Feher, G. *Biochim. Biophys. Acta* **1993**, *1183*, 139−160.

(34) Okamura, M. Y.; Isaacson, R. A.; Feher, G. *Biochim. Biophys. Acta* **1979**, *546*, 394−417.

(35) Lendzian, F.; Bönigk, B.; Plato, M.; Möbius, K.; Lubitz, W. In *The Photosynthetic Bacterial Reaction Center II*; Breton, J., Verméglio, A., Eds.; Plenum Press: New York, 1992.

(36) Chidsey, C. E. D.; Takiff, L.; Goldstein, R. A.; Boxer, S. G. *Proc. Natl. Acad. Sci. U.S.A.* **1985**, *82*, 6850−6854.

(37) Herzfeld, J.; Berger, A. E. *J. Chem. Phys.* **1980**, *73*, 6021−6030.

(38) Schmidt-Rohr, K.; Spiess, H. W. *Multidimensional Solid-State NMR and Polymers*; Academic Press: San Diego, 1996.

(39) Zysmilich, M. G. Ph.D. Thesis, Columbia University, NY, 1997.

(40) Gunner, M. R.; Dutton, P. L. *J. Am. Chem. Soc.* **1989**, *111*, 3400−3412.

(41) Lubitz, W.; Lendzian, F.; Möbius, K. *Chem. Phys. Lett.* **1981**, *84*, 33−38.